Data-driven analysis of a 2D-$E \times B$ kinetic simulation relevant to Hall thruster discharges

IEPC-2024-640

Borja Bayón-Buján[*] , Enrique Bello-Benítez[†] , Jiewei Zhou[‡] and Mario Merino[§]
Department of Aerospace Engineering, Universidad Carlos III de Madrid, Leganés, Spain.

Spectral decomposition and bicoherence analysis of a full-PIC $E \times B$ discharge simulation shows that the majority of the collisionless cross-field transport can be attributed first Electron Cyclotron Drift Instability (ECDI) mode, surpassing the contribution of a longer wavelength mode present in the results, while higher modes of the ECDI exhibit negligible impact. Electron anomalous transport appears to be modulated by a low frequency mode, compatible with the ion residence time in the domain. Bicoherence analysis and sparse regression is then used to identify the non-linear transfer of power among scales in the plasma. A reduced model, based on three-wave coupling equations, is proposed, which indicates the transfer of energy from shorter to longer wavelengths, in an inverse energy cascade. This work provides new insights into the dynamics of anomalous plasma transport and the underlying processes governing energy distribution across different scales.

I. Introduction

$\mathbf{A}$NOMALOUS cross-field electron transport in $\boldsymbol{E} \times \boldsymbol{B}$ plasmas, notably in Hall thrusters, remains a key unexplained phenomenon that drives the performance losses of these devices.[1,2] The significant electron drift in the azimuthal direction of Hall thrusters is known to give rise to various azimuthal oscillations and instabilities, potential explanations for the observed anomalous transport. It is generally agreed that cross-field anomalous transport of electrons occurs mainly due to the $\overline{n_e E_y}$ time-averaged term in the azimuthal momentum equation.[3–5] However, the underlying mechanisms giving rise to these azimuthal oscillations are still a subject of active research. Major candidates are several electrostatic instabilities and/or broad spectrum, developed turbulence.[6–11]

Particle-in-cell (PIC) codes have been widely used to simulate the effect of instability-induced oscillation on Hall plasmas; either in canonical[5,12–16] or more realistic/applied[17–19] scenarios. When wave propagation is limited to the direction perpendicular to the applied magnetic field, the electron cyclotron drift instability (ECDI) has been identified as one of the probable actors behind the anomalous electron transport. Even if the linear theory of the ECDI is well known,[8,9,20,21] the exact mechanisms or transport laws in the nonlinear regime are still a matter of discussion. Some points that need to be further clarified are the suggested development of an inverse-cascade process,[13,15] the transition of the ECDI to an ion-acoustic mode,[14,19] and the interaction of boundary conditions with the nonlinear behavior of the ECDI.[4,5,12,14]

Recently, data-driven techniques have been adapted and tested on electric propulsion plasmas, as a valuable addition to the toolbox of the researcher to provide new insights. These techniques also offer the advantage of being flexible in their applicability. Very recent examples include the use data coming from axial-radial simulations of a Hall discharge to identify and isolate dominant dynamic regimes through Proper Orthogonal Decomposition (POD) and Dynamic Mode Decomposition (DMD);[22–24] further work used one of these

---

*Research Assistant, bbayon@pa.uc3m.es
†PhD Candidate, ebello@ing.uc3m.es
‡Assistant Professor, jzhou@pa.uc3m.es
§Professor, marmerin@ing.uc3m.es

datasets together with the Sparse Identification of Nonlinear Dynamics (SINDy) algorithm[25] to obtain parsimonious equations (both physically-meaningful and with very few terms) of the breathing mode dynamics directly from the time-series of plasma variables. Previously, symbolic regression had also been proposed to obtain data-driven closures to the anomalous transport problem.[26]

Weakly-nonlinear plasma theory treats a perturbation as a superposition of eigenmodes with an amplitude that varies in time due to nonlinear interactions, which can be divided in two main types: wave-wave and wave-particle interactions.[27] Higher order of spectral analysis can be used to delve into wave-wave interactions; particularly, the bicoherence has been used successfully to identify quadratic nonlinear interactions in space plasmas[28] and in fusion plasmas,[29,30] among many other applications. Within electric propulsion, a recent study[31] used this technique to relate low and high-frequency density oscillations in a Hall discharge from microwave interferometry measurements, while another used the bispectrum together with three-wave coupling theory to obtain growth rates and non-linear interaction coefficients from experimental data,[32] identifying the relevant spectral components for instability, albeit based on an mathematically overdetermined problem.

In this paper, we use the full-PIC simulation data of Bello-Benítez et al.[4,12] to first analyze the contribution of the $\overline{n_e E_y}$ term to the cross-field electron current j_{ze}, by examining the frequency spectrum and identifying the primary contributors based on the magnitude and phase difference of the n and E_y oscillations. Next, we investigate the nonlinear coupling between the n, E_y, and j_{ze} time signals through mutual bicoherence analysis. After establishing the dominance of this mechanism in cross-field electron transport, we then build a reduced spectral model for the non-linear energy coupling in the E_y spectrum by means of sparse-regression data-driven modeling of energy evolution at dominant frequencies. Our study identifies the bands responsible for transport and demonstrates that three-wave coupling effectively explains the energy transfer from instability frequencies to bands facilitating cross-field transport. The general methodology used is applicable to other plasma transport studies driven by fluctuations.

The rest of the paper is structured as follows: Section II provides a brief overview of the simulation and the data used to carry out this work, Section III introduces the tools used to analize and model the data, Section IV outlines the results obtained, divided into Section A for the identification of dominant contributions to the anomalous electron current, and B for the reduced models of nonlinear three-wave power energy transfer. Finally, Section V gathers the conclusions of the study as well as future steps.

II.   Simulation overview

Simulations of a canonical $\boldsymbol{E} \times \boldsymbol{B}$ plasma discharge obtained with the in-house, 2D, electrostatic full-PIC code PICASO[4,12,33,34] consitute the dataset used in this work.

The details of the code and the simulations are included in those references. In essence, the equations of motion of the ion and electron macroparticles are solved with a standard Boris algorithm and the interpolation and weighting schemes implement first-order bi-linear shape functions. The code is implemented in Fortran90 and the operations on macroparticles are parallelized following a particle-decomposition strategy using shared-memory OpenMP. The Poisson solver used here employs second-order finite-differences to discretize the Laplace operator and PARDISO Intel MKL direct solver to invert the resulting linear system.

The simulation settings are summarized in Figure 2 and in Table 1. A collisionless plasma composed of electrons and hydrogen ions is considered. The settings aim to replicate essential aspects of the physics needed to trigger and sustain the instability,[4,12] while excluding other factors like field inhomogeneities, ionization, and collisions, as noted in those prior studies. The simulation domain length is chosen such that modes $k_{yn}L_y = n$ with $n = 1 + 6m$ approximately match the linear growth rate peaks associated with each ECDI resonance

A fixed magnetic field $\boldsymbol{B}_0 = B_0 \mathbf{1}_x$ is considered in the out-of-plane direction, together with a perpendicular equilibrium electric field $\boldsymbol{E}_0 = E_0 \mathbf{1}_z$ in the axial direction; where the sub-index '0' stands for *equilibrium conditions* throughout the paper. As usually assumed in Hall thruster plasmas, ions are considered unmagnetized (i.e., they do not feel $\boldsymbol{B}_0$) and consequently an equilibrium is only possible if the effect of $\boldsymbol{E}_0$ on ions is also disregarded. Otherwise, ions would tend to accelerate, inducing significant inhomogeneity in the plasma. It is for this reason that, the unmagnetized ions move according to the electric field $\boldsymbol{E}_i = \boldsymbol{E}_1$, while electrons feel the action of $\boldsymbol{B}_0$ and $\boldsymbol{E}_e = \boldsymbol{E}_0 + \boldsymbol{E}_1$, being $\boldsymbol{E}_1 = -\nabla \phi$ the local fluctuation relative to $\boldsymbol{E}_0$

obtained from the Poisson solution. This approach was followed in previous works and is known to prevent having proper energy conservation.[12,13,15]

The plasma simulation is initiated in homogeneous equilibrium state with cold ions drifting with velocity $\boldsymbol{u}_{i0} = u_{zi0}\mathbf{1}_z$ and Maxwellian electrons with temperature T_{e0} and mean velocity $\boldsymbol{u}_{e0} = u_{ye0}\mathbf{1}_y$, corresponding to the $\boldsymbol{E} \times \boldsymbol{B}$ drift $u_{ye0} = E_0/B_0$. The density of both species is n_0. The initial macroparticle populations of electrons and ions are randomly generated with these properties.

On the upper and lower boundaries, periodic boundary conditions are imposed on the particles and on the potential. Then, direction y mimics the azimuthal direction in a Hall thruster. Particles reaching axial boundaries are removed from the simulation, but there is continuous injection of ions though left boundary with flux density $n_0 u_{zi0}$ and of electrons through left/right boundaries with fluxes $\pm n_0 c_{e0}/\sqrt{2\pi}$; corresponding to equilibrium conditions.

Description and symbol	Value and units
Ion mass, m_i	1 u
Applied electric field, E_0	10^4 V/m
Applied magnetic field, B_0	200 G
Plasma density, n_0	10^{17} m^{-3}
Ion axial velocity, u_{zi0}	10 km/s
Electron temperature, T_{e0}	6 eV
'Azimuthal' domain length, L_y	5.359 mm
Axial domain length, L_z	2.679 mm
$E \times B$ drift, u_{ye0}	500 km/s
Electron thermal speed, c_{e0}	1027 km/s
Ion sound speed, c_{s0}	23.97 km/s
Debye length, λ_{D0}	57.58 μm
Electron Larmor radius, ρ_{e0}	292.0 μm
Electron plasma frequency, ω_{pe0}	2.839 GHz
Electron gyrofrequency, ω_{ce}	0.5600 GHz
Ion plasma frequency, ω_{pi0}	66.26 MHz
Lower-hybrid frequency, ω_{lh}	13.07 MHz
Number of cells in y direction, N_y	100
Number of cells in z direction, N_z	50
Number of particles per cell, N_{ppc}	200
Time step, Δt	5×10^{-12} s
Number of time steps, N_t	6×10^5
Azimuthal cell size, Δy	53.59 μm
Axial cell size, Δz	53.59 μm

Table 1: Physical and numerical parameters of the reference simulation case. The subscript '0' stands for initial equilibrium conditions. Derived parameter values are included for completeness.

In the already-mentioned previous work,[12] unstable short-wavelength modes were observed to grow from the initially homogeneous plasma, quickly evolving into a non-linear stage and then saturating. The electric potential ϕ was also observed to develop fluctuations mainly in the downstream part of the domain. A spatial snapshot of the potential oscillation is shown on the upper left panel of Figure 2. The analysis and modeling in the remainder of this work focus on data from the axial slice shown in Figure 2(a), unless otherwise noted. This slice was chosen because it corresponds to a position where the instability is fully developed. Additionally, initial transient stage of the simulation is disregarded.

Plasma properties and the anomalous current were observed to oscillate in time alternating between periods
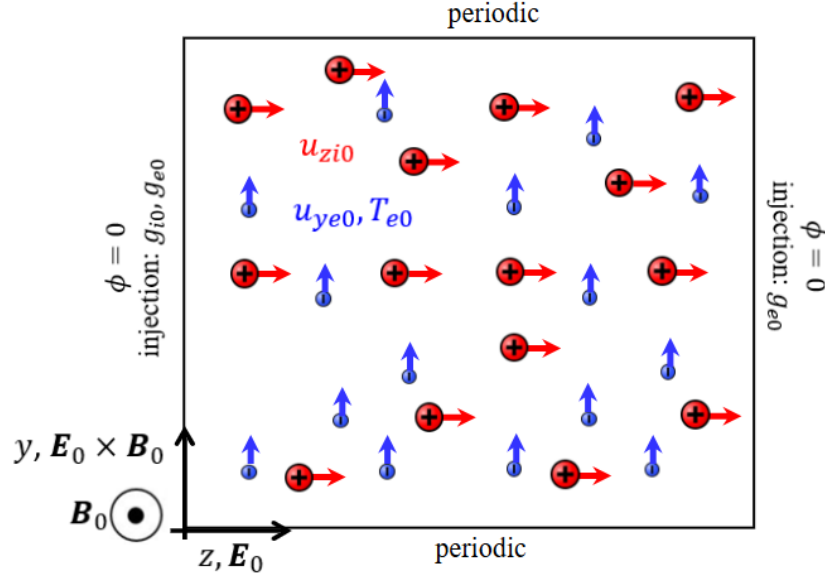
Figure 1: Diagram sketching the full-PIC simulation domain, boundary conditions and initial equilibrium state.

of growth and quenching, modulated by a low frequency compatible with the ion transit time. This is visible in the spectrogram of ϕ in the bottom panel of figure 2, which showcases the time evolution of the azimuthal modes.

The right panel of figure 2 displays the spectral power distribution of ϕ in the (k_y , ω) plane, where an approximately straight dispersion relation can be broadly traced out, although it is complicated by many other mechanisms. Four peaks can be identified, at (1, 20), (7, 42), (13, 84), and (19, 126), given in multiples of L_y and MHz, on this straight line, respectively named modes A to D. An additional relevant mode can be distinguished at $(k_y L_y , \omega$ [MHz]): (0, 1.6), named mode O hereon. Peak broadening is also observed, particularly forming a broadband that extends between modes A and B. Note that the high frequencies compared to those typical of Hall thrusters result from using hydrogen ions in the simulation instead of the usual propellants.

In terms of wavenumber, modes B to D are predicted by ECDI linear theory,[12] while mode A, corresponding to the largest wavemode in the entire azimuthal domain size, is not. Nevertheless, the frequencies of the ECDI modes stray significantly from those predicted by linear theory, having higher frequencies. Indeed, the results from linear theory need not apply in the nonlinear stage.

As a final note, the dispersion map in Figure 2 confirms that, despite mode C being predicted to have the biggest growth rate,[12] mode B quickly dominates the spectrum in terms of energy; this is a clear hint of the existence of nonlinear energy exchanges.

III. Methods

A. High order spectral analysis

Bicoherence, the normalized third-order cumulant spectrum, measures the coupling between modes. It ranges from 0 (no coupling) to 1 (complete coupling) and describes interactions between modes at ω_1, ω_2 and ω_3 where $(\omega_3 = \omega_1 + \omega_2)$.[35] Given the discrete Fourier representation $x_i(t) = \sum X_i(\omega)e^{-j\omega_k t}$ (where the sum extends over the full ω spectrum under consideration), we define

$$b^2(\omega_1, \omega_2) = \frac{|\langle X_a(\omega_1)X_b(\omega_2)X_c^*(\omega_1 + \omega_2)\rangle|^2}{\left\langle |X_a(\omega_1)X_b(\omega_2)|^2 \right\rangle \left\langle |X_c^*(\omega_1 + \omega_2)|^2 \right\rangle}. \tag{1}$$
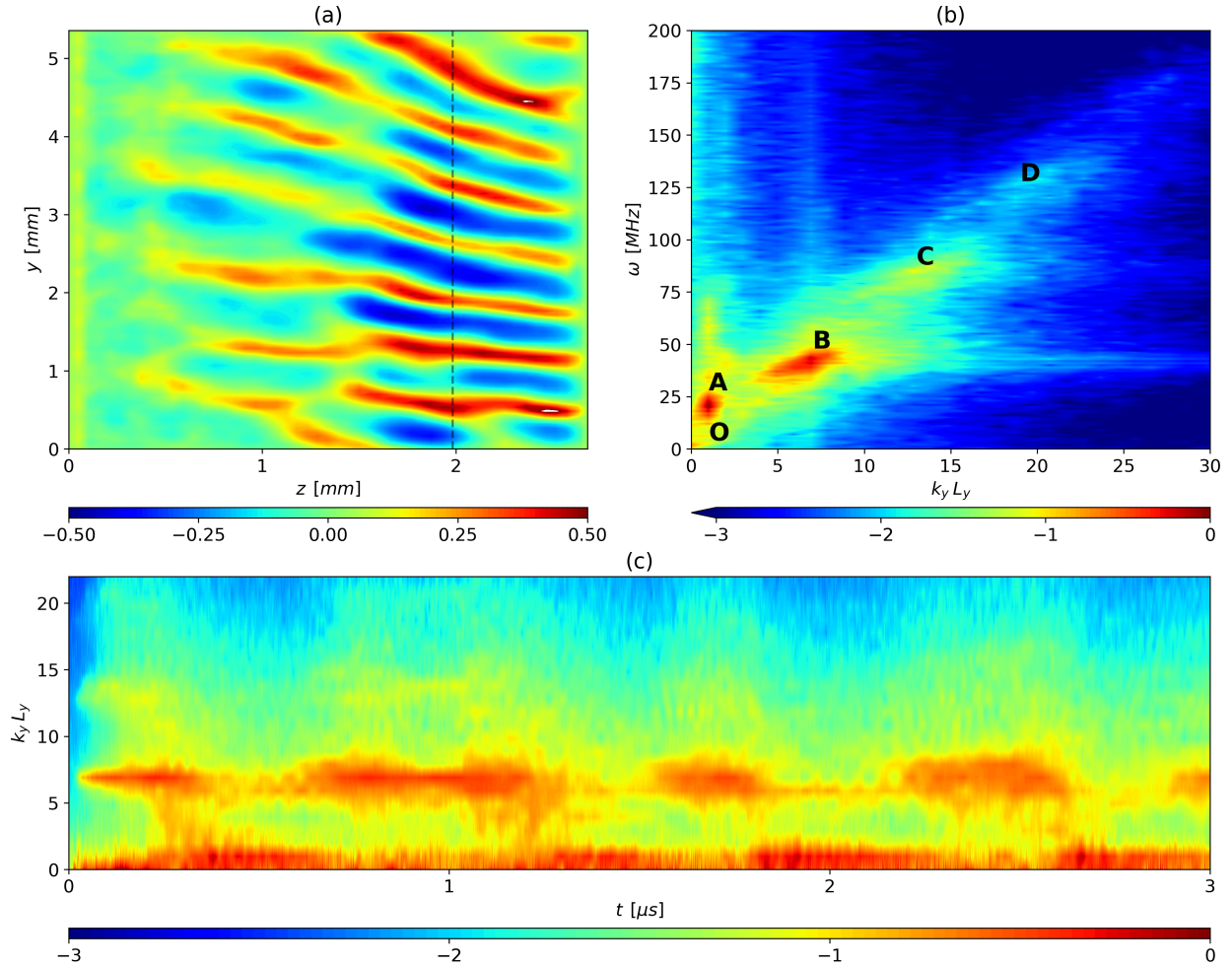
Figure 2: Oscillations of ϕ present in the full-PIC simulation. (a) a spatial snapshot;(b) dispersion in the $\omega-k_y$ plane (c) $t-k_y$ spectrogram. The dotted black line in (a) denotes the axial slice ($z = 1.98mm$) where both the dispersion diagram and spectrogram are computed.

When signals X_a, X_b, and X_c are the same, one speaks of b^2 as the (self-)bicoherence of that signal; otherwise, the term cross-bicoherence (among different signals) is used. Here, $\langle \cdot \rangle$ denotes averaging over multiple realizations, and x^* is the complex conjugate of x. This equation can also be equivalently applied in wavenumber space. A value of 1 indicates perfectly phase-locked modes, suggesting three-wave coupling, whereas random phases or noise will lead to bicoherence values closer to 0 as the number of realizations or the noise level increases.

When it comes to plotting the bicoherence, it is necessary to take notice of the Nyquist limit. In terms of frequency ω only, this is

$$\omega_1, \omega_2, \omega_3 < f_s/2. \tag{2}$$

Equation (2) restricts the computation to a hexagon in the (ω_1, ω_2) plane. Additionally, for the self-bicoherence, there are a number of symmetries in Equation (1). Again, in terms of ω only:

$$b^2(\omega_1, \omega_2) = b^2(\omega_2, \omega_1) = b^2(\omega_1, -\omega_3) = b^2(-\omega_1, -\omega_2), \tag{3}$$

where the last equality assumes real signals. The mentioned symmetries allow to reduce the required computation area to a triangle in the first quadrant for the self-bicoherence.

Discrete interactions between two modes appear as "islands" whose width corresponds to the spectral broadening of interacting peaks. Harmonic interactions typically show as a dotted pattern of equi-spaced islands. Continuous interactions of a single frequency with a broader band are shown as lines or segments, either verticals ($\omega_1 =$), horizontals ($\omega_2 =$) or topleft-bottomright diagonals ($\omega_3 =$).

Identical considerations to all the above apply in terms of $\boldsymbol{k}$ instead of ω, given $x_i(t) = \sum X_i(\boldsymbol{k})e^{j\boldsymbol{k}\cdot\boldsymbol{x}}$.

Note that the bicoherence is high when quadratic coupling exists among modes. However, the bicoherence itself does not discriminate the direction of power flow among them , and this directionality needs to be studied by other methods, such as by identifying the three-wave coupling equations.

B. Sparse Identification of Nonlinear Dynamics (SINDy)

As explained in,[25] the basic form of the Sparse Identification of Non-linear Dynamics (SINDy) framework[36] goes as follows. We consider a dynamical system of state $\boldsymbol{x}(t) = [x_1(t), x_2(t), \ldots, x_I(t)]^T$, in a state space $\mathbb{X}$, governed by a set of ordinary differential equations of the form

$$\dot{x}_i(t) = f_i(\boldsymbol{x}, t), \tag{4}$$

where f_i $(i = 1, \ldots, I)$ are unknown functions of the state, and possibly time. In general, we may write each f_i in (4) as

$$f_i(\boldsymbol{x}, t) = \beta_{ij}\Theta_j(\boldsymbol{x}, t), \tag{5}$$

where Θ_j $(j = 1, \ldots, J)$ is a collection of functions (termed "features") and β_{ij} a (sparse) set of coefficients to be determined.

If a realization of the dynamical system has data $x_i(t_k) \equiv \hat{x}_{ik}$ at discrete time instants t_k $(k = 0, \ldots, K)$, potentially subject to noise, it is possible to estimate the coefficients β_{ij} from the following linear system of equations:

$$\dot{\hat{x}}_{ik} = \beta_{ij}\hat{\Theta}_{jk} \tag{6}$$

where $\dot{\hat{x}}_{ik}$ is a numerical estimate of the state derivatives, e.g. using finite differences, and $\hat{\Theta}_{jk} \equiv \Theta_j(\hat{\boldsymbol{x}}(t_k), t_k)$.

The set of equations is typically strongly overdetermined, as we have many more equations than unknown coefficients, $K \gg IJ$. Naively solving for β_{ij} by minimization of the least-square error

$$\varepsilon^S = \frac{1}{N} \frac{1}{\hat{\sigma}_{\dot{x}}^2} \sum_{i,k} \left(\dot{\hat{x}}_{ik} - \beta_{ij}\hat{\Theta}_{jk} \right)^2, \tag{7}$$

where N stands for the sample size and $\hat{\sigma}_{\dot{x}}^2$ for the variance of the numerical derivatives, typically yields a full β_{ij} matrix where most coefficients are different from zero. This is usually undesired, as the resulting models exhibit an unaffordable complexity and lack simple physical interpretations.

What SINDy proposes is finding β_{ij} through the minimization of the sum of a Least Square error ε^S, plus an sparsity-promoting regularization term, or penalty, ε^λ,

$$\beta_{ij} = \underset{\beta_{ij}}{\operatorname{argmin}} \left(\varepsilon^S + \varepsilon^\lambda \right). \tag{8}$$

By regularizing to promote sparsity in the solution β_{ij}, the algorithm is shown to regress on the features most relevant to the dynamics and discard the rest.[36] In the present work, we use the Adaptive LASSO penalty[37, 38]

$$\varepsilon^\lambda = |a_{ij}\beta_{ij}| \quad \text{with } a_{ij} = \frac{\lambda_i}{\beta_{ij}^*}, \tag{9}$$

where the λ_i are hyperparameters which set the relative weight of the regularization term over the error term for each state variable, and the term-specific weights β_{ij}^* are the coefficient estimates coming from optimizing ε^S alone,

$$\beta_{ij}^* = \underset{\beta_{ij}}{\operatorname{argmin}} \left(\varepsilon^S \right). \tag{10}$$

This form of ε^λ puts a large penalty on small coefficients while reducing biases on the larger coefficients. The ALASSO penalty also has the benefit of leading to a computationally-efficient convex minimization problem. Furthermore, it tends to consistent variable selection and correct coefficient estimation as the number of samples K tends to infinity, given that all relevant features are included in the chosen function library, and available data spans the whole state space sufficiently.[38]

For each state variable x_i sweeping the regularization parameter λ_i from 0 to infinity and plotting the error and complexity results in an L-shaped Pareto front, from which the optimal model can be selected based on the knee inflexion point[39] or researcher insight.

IV. Results

A. Analysis

The azimuthal average $(\bar{\cdot})$ of the azimuthal electron momentum equation (disregarding radial effects and collisions) reads

$$\bar{\jmath}_{ze}(t) = \frac{e}{B}\overline{n_e E_y} - \frac{1}{B}\frac{\partial}{\partial z}\bar{M}_{zye} - \frac{m_e}{B}\frac{\partial}{\partial t}\overline{n_e u_{ey}}, \tag{11}$$

where $\bar{M}_{zye}$ the axial-azimuthal component of the electron momentum tensor. Typically, it is assumed that the first term dominates transport,

$$\bar{\jmath}_{ze}(t) \simeq \frac{e}{B}\overline{n_e E_y}. \tag{12}$$

A net axial current forms when the fluctuations in these two quantities are in phase. Figure 3 showcases how this sole term serves to explain most of the axial transport in our simulation. The difference in current is ascribed to the inertial and gyroviscous terms in equation (11), which act to diminish the total current. A modulating envelope roughly corresponding to 1.6 MHz can be distinguished.

The contribution of the different parts of the fluctuation spectrum to plasma transport is considered next. Following a development similar to Powers,[40] one may express the time-averaged Equation 12 as a sum over frequencies,

$$\langle \bar{\jmath}_{ze} \rangle = \frac{e}{B} \left\langle \overline{n_e E_y} \right\rangle = \frac{2e}{B} \int_0^\infty \left| P_{n_e E_y}(\omega) \right| \cos(\alpha_{n_e E_y}(\omega)) d\omega \tag{13}$$

Here, $\langle \cdot \rangle$ denotes time-averaging over a window, the same window from which the spectral components are computed. For a mode with frequency ω to contribute to transport, it is necessary for its product inside Equation 13 to be significant.

Figure 4 shows the cross spectral density (CSD) magnitude and cosine in our simulation. The peaks corresponding to mode A ($\simeq 20$ MHz), mode B ($\simeq 40$ MHz) and mode C ($\simeq 80$ MHz) are easily identifiable. In terms of phase couplings, the entire range up to 100 MHz seems to have a coherent phase and is able to contribute to the plasma transport. It is noticeable that for most of this interval the phase is nearly constant and approximately $80°$, i.e. the value of the cosine is not large. However, the cross-spectral density
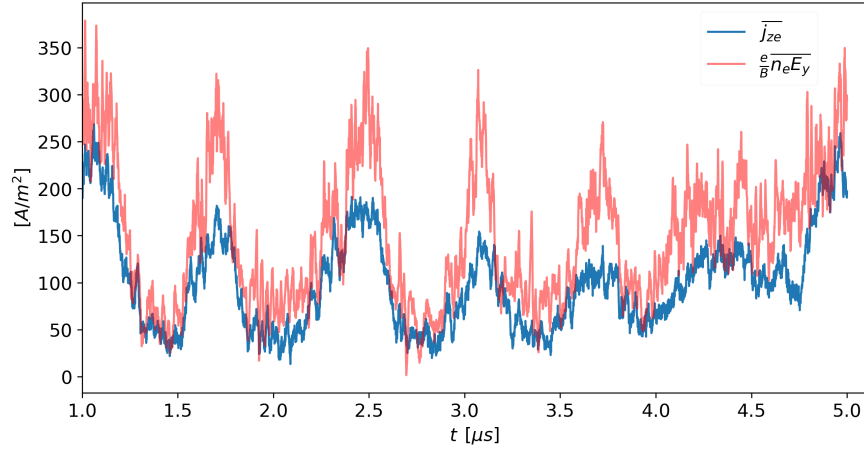
Figure 3: Time-evolution of the y-averaged electron axial current compared to the current induced by the n_e, E_y fluctuations.
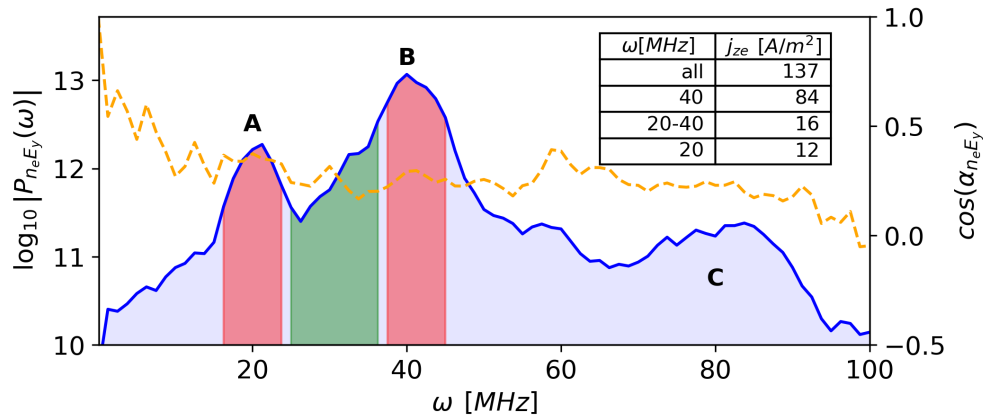

Figure 4: Cross-spectral density and cosine of angle between n_e and E_y, reflecting the spectral contribution to j_{ze}. The table showcases the resulting current from integrating in each shaded area. A, B, C correspond to the peaks identified in figure 2.

for the peaks corresponding to modes A and B is significant, and integrating Equation 13 for their specific frequency bands, we see that mode B contributes approximately 65% of the current while mode A contributes about 10%. The latter is comparable to the contribution of the intermediate range between these two peaks. The other frequencies do not carry enough power to yield significant contributions even if the corresponding phase difference approaches 0°, while the range above 100 MHz (not shown in the figure) has an erratic phase difference and so does not contribute substantially either. On a final note, locations at other z positions, upstream of the domain (where the ECDI is not as well-developed), show the same trends but with a higher contribution of the 20-40MHz band to transport, which becomes significant.
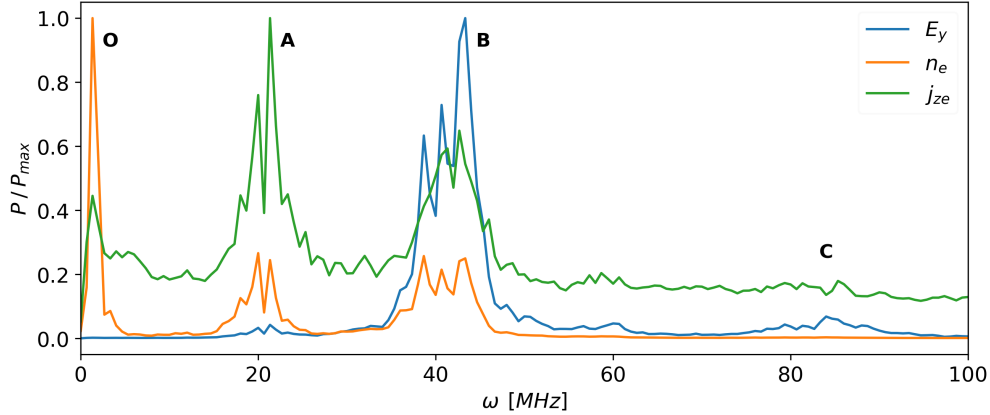

Figure 5: Power spectral density of n_e, E_y, j_{ze}, normalized by their corresponding maximum values, and taken from the axial slice downstream. O, A, B, C correspond to the peaks identified in figure 2.

Extending the analysis to the Power Spectral Density (PSD) of the relevant variables, it can be seen from Figure 5 that they all practically showcase the same modes as ϕ, albeit with differing amplitudes for each mode, with the dominant one being different for each variable. Indeed, the PSD of j_{ze} is dominated by mode A, while E_y features prominently mode B, and n_e mode 0. We note that, while $P_{E_y} = k_y P_\phi$ holds, the absence of mode O in the E_y spectra highlights that this mode is fundamentally axial. The axial character of mode O and the similarity, from Table 1, of $u_{zi}/L_z = 0.9 \times 10^6$ s^{-1} to the mode's frequency, hints at a relation with the ion transit time. Other simulations with different input parameters show that the mode frequency scales as $1/\sqrt{m_i}$ similar to the rest of the spectra, but does not depend on n_e. However, changing the injection velocity u_{zi0} does not yield the expected linear change in frequency. This discrepancy can be linked to the sensibility of the resulting simulation dynamics to this parameter, as explored in previous works.;[12] however, this link of the mode with the ECDI saturation makes us conclude that this could be a more complicated version of the classical ITT instability.

The multi-peaked structure of modes A and B, suggests some form of nonlinear modulation, likely by mode O. Indeed, as observed in the spectrogram on the bottom panel of figure 2, the maxima of the amplitude of the ECDI modes B and C alternate in time with that of mode A (periods that we refer to as "quenching"), with a repetition frequency roughly equal to that of mode O. The spectrum between modes seems to gain some importance at the end of each cycle of large ECDI modes. This time alternation in the dominant mode corresponds as well with the modulation of j_{ze}, whose maxima corresponde to maxima of modes B and C, as seen in Figure 3.

Given this alternation of mode A with modes B, C in time, we examined whether the results shown in Figure 4 also varied over time, were the PSDs to be computed in windows at the maxima of mode A or at the maxima of modes B, C. Our analysis indicates that the small transport contribution linked to mode A primarily occurs during the "quenching" period, where nevertheless anomalous transport is at its minimum. This underscores the limitations of relying solely on stationary spectra.

It is important to acknowledge the possibility that modes not directly contributing to transport may still be instrumental in coupling and transferring energy nonlinearly from/to contributing modes. Bicoherence analysis examines the possible nonlinear couplings between modes and frequency bands in terms of relative phase locking, identifying relevant frequencies for modeling. Given the distinct spectra for n_e and E_y

discussed earlier, studying the self-bicoherence of these variables, along with their cross-bicoherence with j_{ze}, can help elucidate how different modes interact to transfer energy.
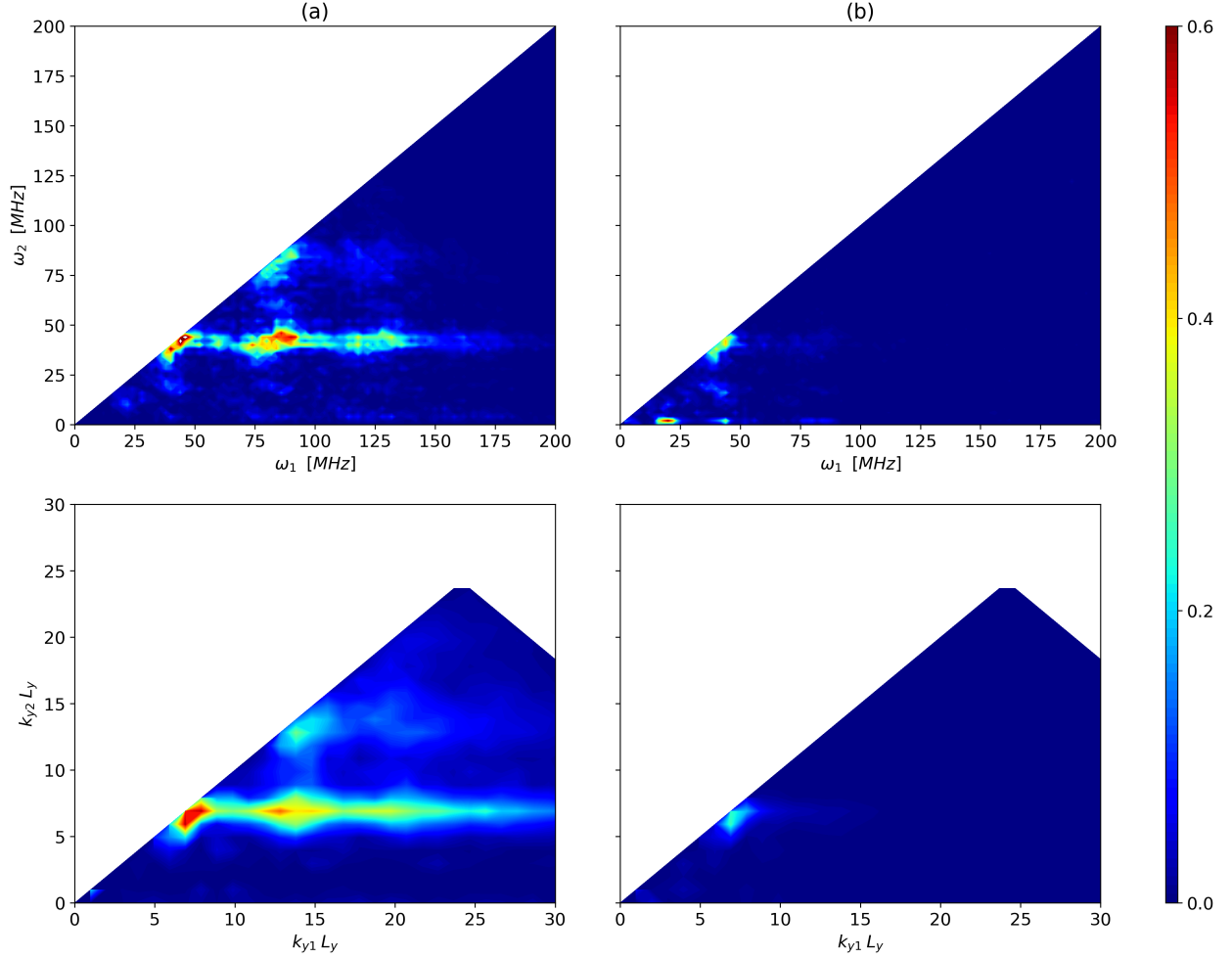

Figure 6: a) Self-bicoherence of E_y, b) Self-bicoherence of n_e. White space denotes the redundant or inaccessible areas. Upper plots are in ω; lower plots in k_y.

Figure 6 showcases the self-bicoherence for the first two variables in terms of ω and k_y. For E_y, a strong structure linked to the interaction of ECDI modes B, C and D is visible. This could hint of an energy cascade process. However, the direction of the power flow cannot be determined from this analysis alone. We note that the resonance conditions $\omega = \omega_1 + \omega_2$ and $k = k_1 + k_2$, needed for three-wave coupling to exist, are fulfilled in a broad sense, in particular when the broadening of the cyclotron resonances is taken into account. This is in contrast to the findings from linear theory, where the wavenumbers and frequencies for each instability peak are not exact multiples of each other.[12]

Significantly weaker interactions are seen along the 1.6 MHz and 20 MHz lines, representing the modulation of modes O and A, respectively, over the remaining modes. On the other hand, for n_e the strongest interactions are the modulation of modes A and B by mode O, visible in the diagram in ω space, followed by the interaction of mode B with C. There is also a small peak corresponding to energy transfer between 40 MHz, 20 MHz and 60 MHz.

The cross-bicoherence among the three variables can be seen in the (ω_1, ω_2) plane in Figure 7. Given that the previous analysis shows that the bicoherence carries essentially the same information in ω and k_y, the latter is not shown. The crucial part of this diagram is the dashed white line, where the n_e modes couple with the E_y modes of same (but negative) frequency to transfer power to/from the $\omega = 0$ j_{ze}, which defines anomalous transport. On this line small bicoherence islands with $b^2 \approx 0.1$ exist at modes A, B and C. This line is
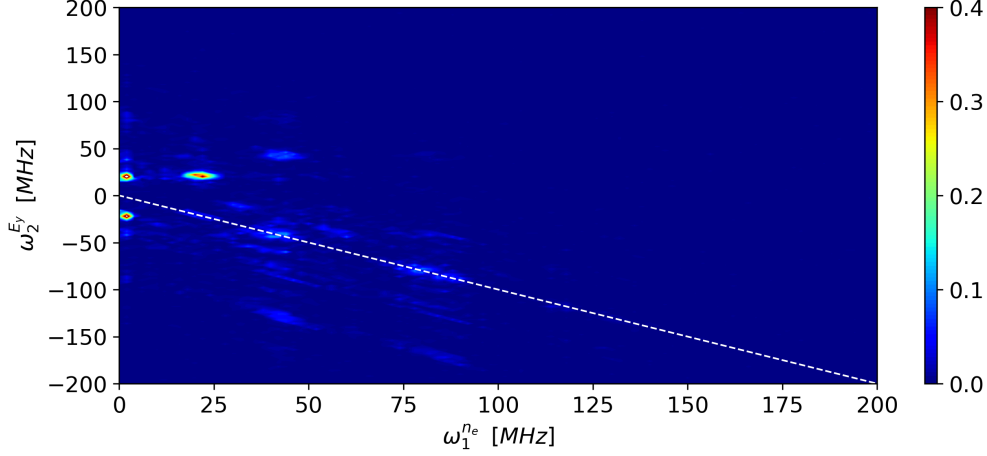
Figure 7: Cross-bicoherence of n_e, E_y, and j_{ze}^* in ω space. The white line denotes the places where the oscillations in n_e and E_y nteract with the DC component of j_{ze}, $\omega_1 + \omega_2 = 0$.

consistent to the one of the CSD of Figure 4, except that the inherent normalization in the definition of the bicoherence makes mode C comparable to the other two. The diagram shows stronger phase-locking islands at $(1.6, \pm 20)MHz$ and at $(20, 20)$ MHz. While these peaks do not represent interactions with the DC part of j_{ze}, they give rise to the seen modulation, and may nevertheless be of importance in finite domains, where AC components of j_{ze} may be rectified by the boundary conditions (which introduce additional nonlinearities) and further contribute to the DC anomalous transport.

B. Modeling - reduced spectral model

Bicoherence serves as an indicator of the amount of non-linear energy transfer than can be explained by three-wave coupling interactions. However, it cannot discriminate the directionality of the flow of energy, and may also be affected by coincidental phase-locking conditions not related to nonlinear power transfer. In this section, a reduced model of the most relevant modes for axial electron transport will be obtained. The approach can be regarded as a data-driven, sparsity-promoting, shrinked-down version of the Kim-Ritz method[41, 42] which was used in other studies,[32] with significantly fewer modes and terms per equation. The electric field will be taken into consideration once more, as despite storing less energy than the electron density, features a stronger correlation among modes B, C, D as seen in figure 6.

To extract the time series for the mode amplitudes, we select a region around each (k, ω) space representing the broadened modes B, C, D and compute the windowed PSD in time. The square root of the PSD, that is the absolute value of the signal magnitudes, is retained. The computation window is then displaced in prescribed timesteps to obtain the time evolution of the amplitudes. Since the window must cover multiple cycles of the relevant frequencies for energy transfer over longer scales, we use a simulation with the same inputs described in Table 2 but run for $30\mu s$. The initial transient startup period is discarded. We choose a window spanning $1.4\mu s$ with a step of $0.3\mu s$, utilizing the same axial slice used in the rest of this work to obtain the models.

To apply the SINDy algorithm, we then build a limited feature library that includes linear growth rate terms, axial convection terms, and the relevant three-wave coupling terms for the wave amplitude.[27] For each mode $i = B, C, D$ then,

$$\frac{\partial}{\partial t}|X_i| = \gamma|X_i| - v_{gi}\frac{\partial}{\partial z}|X_i| + \sum_{j^*, k^*} V_{ijk}|X_j X_k|, \tag{14}$$

The coefficients on the right-hand side, to be determined, are the linear growth with growth rate γ_i, the group velocity v_{gi}, and the sum of wave-wave interactions with coupling coefficients V_{ijk}, for each mode. The sum of the latter extends to values of j, k that yield a valid resonant triad with i. Note that the resonance condition also accounts for negative frequencies; for example, for the frequency triplet $\omega_1 = 80MHz$, $\omega_2 = -40MHz$,

$\omega = 40MHz$, mode B can interact with mode C to either transfer or receive energy, depending on the sign of the coefficient. In our absolute-value model, these details become irrelevant.

n_{terms}	Model
1	$\partial E_y^B/\partial t = 6.27 \cdot 10^{-4} E_y^B E_y^C$
2	$\boldsymbol{\partial E_y^B/\partial t = -4.36 \cdot 10^5 E_y^B + 4.45 \cdot 10^{-3} E_y^B E_y^C}$
3	$\partial E_y^B/\partial t = -4.60 \cdot 10^5 E_y^B + 4.53 \cdot 10^{-3} E_y^B E_y^C - 1.70 \cdot 10^4 \partial E_y^B/\partial z$
4	$\partial E_y^B/\partial t = -4.32 \cdot 10^5 E_y^B + 3.67 \cdot 10^{-3} E_y^B E_y^C + 1.44 \cdot 10^{-2} E_y^C E_y^D - 1.99 \cdot 10^4 \partial E_y^B/\partial z$
1	$\partial E_y^C/\partial t = -3.09 \cdot 10^{-5} E_y^B E_y^B$
2	$\boldsymbol{\partial E_y^C/\partial t = 2.97 \cdot 10^5 E_y^C - 8.32 \cdot 10^{-5} E_y^B E_y^B}$
3	$\partial E_y^C/\partial t = 3.10 \cdot 10^5 E_y^C - 8.17 \cdot 10^{-5} E_y^B E_y^B - 1.34 \cdot 10^{-4} E_y^B E_y^D$
4	$\partial E_y^C/\partial t = 3.17 \cdot 10^5 E_y^C - 8.30 \cdot 10^{-5} E_y^B E_y^B - 1.24 \cdot 10^{-4} E_y^B E_y^D - 9.81 \cdot 10^2 \partial E_y^C/\partial z$
1	$\partial E_y^D/\partial t = -2.36 \cdot 10^{-5} E_y^B E_y^C$
2	$\boldsymbol{\partial E_y^D/\partial t = 2.17 \cdot 10^5 E_y^D - 9.49 \cdot 10^{-5} E_y^B E_y^C}$
3	$\partial E_y^D/\partial t = 1.71 \cdot 10^5 E_y^D - 9.23 \cdot 10^{-5} E_y^B E_y^C - 9.23 \cdot 10^{-5} \partial E_y^D/\partial z$

Table 2: Pareto front models for modes B, C, D, obtained by sparse regression. E_y^i denotes the absolute value of the complex amplitude of mode i. Terms in red are associated to linear growth/decay rates; orange designates convection terms; blue and cyan terms highlight related wave-wave couplings terms across the modes. The Pareto-optimal models are highlighted in **bold**.

A Pareto front, or hierarchy, of increasingly more complex models for each mode is obtained and displayed in table 2. In bold we have highlighted our identified Pareto knee models, which balance complexity with model error.

While the training data is limited and these results are considered preliminary, and the maximal score of this very-reduced model is low (ranging between 3% and 14%, as determined from Equation 7) , we focus our attention on the sign and order of magnitude of the γ_i and V_{ijk} coefficients; in each equation, positive/negative signs indicate energy flowing in/out of the mode, respectively.

In the models for modes B and C, the dominant term (and therefore the first that shows up in the hierarchy) is the coupling term for the triad BBC, which would transfer energy from mode C into mode B. The term coupling modes BCD appears first in the model for mode D, and also shows up for models more complex than the Pareto-optimal ones for B and C. This term would convey energy from D and C and into B. The sign structure of the couplings BBC and BCD suggest an inverse energy cascade, where energy of the higher-frequency, higher-k modes flows toward lower-frequency, lower-k modes. Unfortunately, no agreement is found on the order of magnitude of the corresponding coefficients for the three modes in either case.

From the analysis of the linear growth rate coefficients γ_i, a general picture emerges: modes C and D receive energy from the ECDI instability, which is then transferred to the longer-scale mode B. The negative growth rate of mode B can be attributed to a net energy loss between what it gains from the instability and what it loses to generating anomalous plasma transport. Finally, convection plays an overall minor role, at least in the selected axial slice, as these terms appear later in the hierarchies.

A sensitivity analysis was conducted for a range of $\pm 0.05\mu s$ of window and step sizes on these results, and the coefficients and the conclusions drawn were found to stable. However, beyond this range, the variability suggests that the intermittent nature of the problem complicates describing interactions without time-varying parameters.

V. Conclusions

This study presented a data-driven analysis of a 2D-$E \times B$ kinetic simulation highlighting the dominance of Electron Cyclotron Drift Instability mode in anomalous electron transport. Higher-order spectral techniques revealed nonlinear power transfer among scales, leading to a reduced model based on three-wave coupling equations showing an inverse energy cascade.

Anomalous transport was found to be mainly driven by in-phase density and electric field fluctuations of the main ECDI mode, while its interactions with the remaining modes warranted further research. Notably, a long mode spanning the azimuthal domain modulated ECDI modes and dominated the current spectra, though its origin remains unclear. A mode related to ion transit influenced the current's quasi-periodicity without significantly affecting energy dynamics.

Bicoherence was used to identify the main nonlinear interactions between modes, while sparse regression expanded this analysis to obtain a hierarchy of data-driven reduced spectral models for the ECDI modes. Both methods served to preliminarily set wave-wave interactions as one of the energy exchange mechanism, where the direction of energy transfer was verified to be that of an inverse energy cascade.

Future work should refine the modeling approach to apply to other parametric regimes and configurations of Hall thrusters, considering field gradients, collisions, and radial effects, and especially, to experimental data. Further examination of temporal localization of couplings, axial distribution of modes, and broadband contributions to current, along with enhancements in methodology such as wavelet analysis and statistical significance tests, could provide more robust insights.

Acknowledgments

References

[1] Kaganovich, I. D., Smolyakov, A., Raitses, Y., Ahedo, E., Mikellides, I. G., Jorns, B., Taccogna, F., Gueroult, R., Tsikata, S., Bourdon, A., Boeuf, J.-P., Keidar, M., Powis, A. T., Merino, M., Cappelli, M., Hara, K., Carlsson, J. A., Fisch, N. J., Chabert, P., Schweigert, I., Lafleur, T., Matyash, K., Khrabrov, A. V., Boswell, R. W., and Fruchtman, A., "Perspectives on Physics of ExB Discharges Relevant to Plasma Propulsion and Similar Technologies," *Physics of Plasmas*, Vol. 27, No. 12, 2020, pp. 120601.

[2] Boeuf, J., "Tutorial: Physics and modeling of Hall thrusters," *J. Applied Physics*, Vol. 121, No. 1, 2017, pp. 011101.

[3] Janes, G. and Lowder, R., "Anomalous electron diffusion and ion acceleration in a low-density plasma," *Physics of Fluids*, Vol. 9, No. 6, 1966, pp. 1115–1123.

[4] Bello-Benítez, E., Marín-Cebrián, A., Ramos, J. J., and Ahedo, E., "Two-dimensional kinetic simulation of electrostatic instabilities in a Hall plasma," 37th *International Electric Propulsion Conference*, No. IEPC-2022-314, Electric Rocket Propulsion Society, Boston, MA, June 19-23, 2022.

[5] Lafleur, T., Baalrud, S., and Chabert, P., "Theory for the anomalous electron transport in Hall effect thrusters. I. Insights from particle-in-cell simulations," *Physics of Plasmas*, Vol. 23, 2016, pp. 053502.

[6] Ramos, J. J., Bello-Benítez, E., and Ahedo, E., "Local analysis of electrostatic modes in a two-fluid E x B plasma," *Physics of Plasmas*, Vol. 28, No. 5, 2021, pp. 052115.

[7] Smolyakov, A., Chapurin, O., Frias, W., Koshkarov, O., Romadanov, I., Tang, T., Umansky, M., Raitses, Y., Kaganovich, I., and Lakhin, V., "Fluid theory and simulations of instabilities, turbulent transport and coherent structures in partially-magnetized plasmas of ExB discharges," *Plasma Physics and Controlled Fusion*, Vol. 59, 2017, pp. 014041.

[8] Forslund, D., Morse, R., and Nielson, C., "Electron cyclotron drift instability," *Physical Review Letters*, Vol. 25, 1970, pp. 1266–1270.

[9] Wong, H., "Electrostatic electron-ion streaming instability," *Physics of Fluids*, Vol. 13, 1970, pp. 757–760.

[10] Litvak, A. and Fisch, N., "Resistive instabilities in Hall current plasma discharge," *Physics of Plasmas*, Vol. 8, No. 2, 2001, pp. 648–651.

[11] Esipchuk, Y. and Tilinin, G., "Drift instability in a Hall-current plasma accelerator," *Sov. Physics-Tech. Physics*, Vol. 21, No. 4, 1976, pp. 417–423.

[12] Bello-Benítez, E., Marín-Cebrián, A., and Ahedo, E., "Effect of injection conditions on the non-linear behavior of the ECDI and related turbulent transport," 2024, Pre-print available at https://arxiv.org/pdf/2405.08761.

[13] Janhunen, S., Smolyakov, A., Chapurin, O., Sydorenko, D., Kaganovich, I., and Raitses, Y., "Nonlinear structures and anomalous transport in partially magnetized ExB plasmas," *Physics of Plasmas*, Vol. 25, 2018, pp. 11608.

[14] Asadi, Z., Taccogna, F., and Sharifian, M., "Numerical Study of Electron Cyclotron Drift Instability: Application to Hall Thruster," *Frontiers in Physics*, Vol. 7, 2019.

[15] Tavassoli, A., Papahn Zadeh, M., Smolyakov, A., Shoucri, M., and Spiteri, R. J., "The electron cyclotron drift instability: A comparison of particle-in-cell and continuum Vlasov simulations," *Physics of Plasmas*, Vol. 30, No. 3, 2023, 033905.

[16]Chen, L., Kan, Z.-C., Gao, W.-F., Duan, P., Chen, J.-Y., Tan, C.-Q., and Cui, Z.-J., "Growth mechanism and characteristics of electron drift instability in Hall thruster with different propellant types," *Chinese Physics B*, Vol. 33, No. 1, 2024, pp. 015203.

[17]Charoy, T., Boeuf, J. P., Bourdon, A., Carlsson, J. A., Chabert, P., Cuenot, B., Eremin, D., Garrigues, L., Hara, K., Kaganovich, I. D., Powis, A. T., Smolyakov, A., Sydorenko, D., Tavant, A., Vermorel, O., and Villafana, W., "2D axial-azimuthal particle-in-cell benchmark for low-temperature partially magnetized plasmas," *Plasma Sources Science and Technology*, Vol. 28, No. 10, 2019, pp. 105010.

[18]Adam, J., Herón, A., and Laval, G., "Study of stationary plasma thrusters using two-dimensional fully kinetic simulations," *Physics of Plasmas*, Vol. 11, 2004, pp. 295–305.

[19]Lafleur, T. and Chabert, P., "The role of instability-enhanced friction on 'anomalous' electron and ion transport in Hall-effect thrusters," *Plasma Sources Science and Technology*, Vol. 27, 2017, pp. 015003.

[20]Ducrocq, A., Adam, J., Héron, A., and Laval, G., "High-frequency electron drift instability in the cross-field configuration of Hall thrusters," *Physics of Plasmas*, Vol. 13, 2006, pp. 102111.

[21]Cavalier, J., Lemoine, N., Bonhomme, G., Tsikata, S., Honoré, C., and Grésillon, D., "Hall thruster plasma fluctuations identified as the ExB electron drift instability: Modeling and fitting on experimental data," *PoP*, Vol. 20, No. 8, 2013, pp. 082107.

[22]Maddaloni, D., Domínguez-Vázquez, A., Terragni, F., and Merino, M., "Data-driven analysis of oscillations in Hall thruster simulations," *Plasma Sources Science and Technology*, Vol. 31, No. 4, apr 2022, pp. 045026.

[23]Perales-Díaz, J., Domínguez-Vázquez, A., Fajardo, P., and Ahedo, E., "Simulations of driven breathing modes of a magnetically shielded Hall thruster," *Plasma Sources Science and Technology*, Vol. 32, No. 7, 2023, pp. 075011.

[24]Faraji, F., Reza, M., Knoll, A., and Kutz, J. N., "Dynamic mode decomposition for data-driven analysis and reduced-order modeling of E× B plasmas: I. Extraction of spatiotemporally coherent patterns," *Journal of Physics D: Applied Physics*, Vol. 57, No. 6, 2023, pp. 065201.

[25]Bayón-Buján, B. and Merino, M., "Data-driven sparse modeling of oscillations in plasma space propulsion," *Machine Learning Science and Technology (under review)*, 2024.

[26]Jorns, B., "Predictive, data-driven model for the anomalous electron collision frequency in a Hall effect thruster," *Plasma Sources Science and Technology*, Vol. 27, No. 10, 2018, pp. 104007.

[27]Sagdeev, R. Z., Galeev, A. A., O'Neil, T. M., and Book, D. L., "Nonlinear plasma theory," 1969.

[28]Lagoutte, D., Lefeuvre, F., and Hanasz, J., "Application of Bicoherence Analysis in Study of Wave Interactions in Space Plasma," *Journal of Geophysical Research*, Vol. 94, 01 1989, pp. 435–442.

[29]Nagashima, Y., Itoh, K., Itoh, S.-I., Hoshino, K., Fujisawa, A., Ejiri, A., Takase, Y., Yagi, M., Shinohara, K., Uehara, K., Kusama, Y., and group, J.-M., "Observation of coherent bicoherence and biphase in potential fluctuations around geodesic acoustic mode frequency on JFT-2M," *Plasma Physics and Controlled Fusion*, Vol. 48, No. 5A, apr 2006, pp. A377.

[30]van Milligen, B., Kalhoff, T., Pedrosa, A., and Hidalgo, C., "Bicoherence during confinement transitions in the TJ-II stellarator," *Nucl. Fusion*, Vol. 48, 11 2008, pp. 115003.

[31]Yamamoto, N., Kuwabara, N., Kuwahara, D., Cho, S., Kosuga, Y., and Dif Pradalier, G., "Observation of plasma turbulence in a hall thruster using microwave interferometry," *Journal of Propulsion and Power*, Vol. 39, No. 6, 2023, pp. 849–855.

[32]Brown, Z. A. and Jorns, B. A., "Growth and saturation of the electron drift instability in a crossed field plasma," *Physical Review Letters*, Vol. 130, No. 11, 2023.

[33]Marín-Cebrián, A., Bello-Benítez, E., Domínguez-Vázquez, A., and Ahedo, E., "Non-Maxwellian electron effects on the macroscopic response of a Hall thruster discharge from an axial–radial kinetic model," *Plasma Sources Science and Technology*, Vol. 33, No. 2, feb 2024, pp. 025008.

[34]Bello-Benítez, E., *Analysis of turbulent transport in Hall-effect plasma thrusters*, Ph.D. thesis, Universidad Carlos III de Madrid, Leganés, Spain, 2024.

[35]Kim, Y. C. and Powers, E. J., "Digital Bispectral Analysis and Its Applications to Nonlinear Wave Interactions," *IEEE Transactions on Plasma Science*, Vol. 7, 1979, pp. 120–131.

[36]Brunton, S. L., Proctor, J. L., and Kutz, J. N., "Discovering governing equations from data by sparse identification of nonlinear dynamical systems," *Proceedings of the National Academy of Sciences*, Vol. 113, No. 15, 2016, pp. 3932–3937.

[37]Cortiella, A., Park, K.-C., and Doostan, A., "Sparse identification of nonlinear dynamical systems via reweighted L1-regularized least squares," *Computer Methods in Applied Mechanics and Engineering*, Vol. 376, 2021, pp. 113620.

[38]Zou, H., "The Adaptive Lasso and its Oracle Properties," *Journal of the American Statistical Association*, Vol. 101, No. 476, 2006, pp. 1418–1429.

[39]Hansen, P. C., "Analysis of discrete ill-posed problems by means of the L-curve," *SIAM Review*, Vol. 34, No. 4, 1992, pp. 561–580.

[40]Powers, E. J., "Spectral techniques for experimental investigation of plasma diffusion due to polychromatic fluctuations," *Nuclear Fusion*, Vol. 14, 1974, pp. 749 – 752.

[41]Kim, J. S., Durst, R. D., Fonck, R. J., Fernandez, E., Ware, A., and Terry, P. W., "Technique for the experimental estimation of nonlinear energy transfer in fully developed turbulence," *Physics of Plasmas*, Vol. 3, No. 11, 11 1996, pp. 3998–4009.

[42]Ritz, C. P., Powers, E. J., and Bengtson, R. D., "Experimental measurement of three-wave coupling and energy cascading," *Physics of Fluids B: Plasma Physics*, Vol. 1, No. 1, 01 1989, pp. 153–163.